International Journal of Computational Vision and Biomechanics
Vol.2 No. 1 (January-June, 2016)

MUK PUBLICATIONS
Open Access Publisher

Micro-Mechanical Modeling of the Mechanosensation of Bone Cells

Adam Lodygowski[1], Udo Nackenhorst[2], George Z. Voyiadjis[1]

[1]*Department of Civil and Environmental Engineering Louisiana State University, Baton Rouge, LA 70803, USA*

[2]*Institute of Mechanics and Computational Mechanics University of Hanover, Hanover 30167, Germany*

The aim of this work is to study the mechanosensation mechanism and the reaction of bone tissue to external loads. The strain detection called mechanosensation is further responsible for bone remodeling which is the process of formation and resorption of bone tissue. To calculate the displacement, strains and stresses the homogenization methods are used. Material properties are derived from the nano length scale. The computations of mechanical models with geometral and material properties, obtained from the literature, are carried out with use of ABAQUS and MSC. PATRAN commercial software. Several models of osteons, structural component of bone responsible for its characteristic mechanical properties, are prepared on a micro length scale.

The results show how crucial is the exactness of the biological geometry modeling. The most satisfactory are the results obtained for the model with the most adequate shape of the biological reality. The strain values computed in the osteocytes – bone cells responsible for the strain detection in bone tissue, are in agrement with the medical theory and experiments. Moreover, it is confirmed that the main contribution to a total strain derives from the osteon longitudinal ε_z strain component.

1. INTRODUCTION

The goal of this study is to contribute to the remodeling simulation of bone tissue. This can be achieved after understanding the mechanosensation of bone cells. The presented work is focused on the micro length scale but, the homogenised results might be of a great importance to the specification of bone's growth and remodeling. The better understanding of problems like implantation of hip-joint-prosthesis (Ebbecke and Nackenhorst (2003)) or osteoporosis (Mullender *et al.* (1996)) and the cooperation of the engineers with medical professionals will lead to the improvement in diagnostics and the decrease in the often painful healing of bone fractures.

Nowadays, numerous simulations based on computational methods and clinical observations are carried out (Ebbecke and Nackenhorst (2003)). However, these kind of calculations cannot take into consideration all processes which occur at the microscale. Especially the process of detecting the external forces by bone tissue namely *mechanosensation*. It is certain that the network of *osteocytes* is responsible for detecting the external loading, however, sending signals to other cells in order to remodel the bone is not yet known (You *et al.* (2001)). The latest results (Lenz and Nackenhorst (2003)) describe these relations between the mechanical loading and strain detection in bone tissue and give a better view over most length scales (nano-micro-meso).

The hierarchical structure is of a great importance in this work. It helps to identify on which of the length scales need to be carried out the modeling process. The most important bone components for the mechanical simulation are briefly introduced. Further on the biomechanic of skeletal adaptation is presented along with several theories concerning this process. Next, the continuum mechanics concepts (kinematics, tensor description) as well as the constitutive relations (linear isotropy and transversal orthotropy) are presented.

Finally the simulation of the living tissues is presented. Formulation of the model requires wide knowledge in both mechanical and biological fields. In order to obtain the geometry which would describe the biological reality in the proper way, it is necessary to use all available medical methods including e.g. micro tomographic pictures. The exactness of the biological geometry was carefully studied in this work and significantly improved in comparison to previous research. Knowing the geometry of the objects under consideration along with the bone tissue behavior under mechanical loading it is possible to attempt the modeling process.

The main goal of this work is to create a three dimensional model of a single osteon and numerical simulation of the selected boundary value problems that reflect the micro strain distribution responsible for the remodeling of bone tissue on the micro level. The complexity of the task as in three dimensional geometrical modeling and numerical computations, requires strong computational environment of the most advanced preprocessors and solvers.

The mechanical approach is carried out in a typical engineering way. The model is prepared and computed with the use of standard engineering software. The

complexity of the modeled structure requires Finite Element Model analysis. The detailed description of the modeling approach is given. Several models with different material properties and shapes of bone cells responsible for the strain detection are presented. Obtained results (strain, stress and displacement visualization) are shown and compared with existing theories ((Frost (1992), You *et al.* (2001)), the fluid-flow theory (Cowin (2002), Turner and Pavalko (1998)), streaming potentials theory (Korenstein *et al.* (1984)) and damage-repair theory (Doblare and Garcia (2002)). A brief summary of the models and results along with the concluding remarks is given and future perspectives are suggested.

2. BIOLOGICAL BACKGROUND

Human's skeleton is like a very complex building. It determines the shape of the body, protects the organs and works closely together with the muscular system to allow us to move. There are 206 bones which build up a skeleton. It means that all these components must function and cooperate properly in order to create a structure which will handle all external, sometimes extreme, loading conditions. In order to provide such conditions it is crucial to understand the behavior and structure of a single skeleton's component.In the following section a multiscale bone structure is presented and an overview of the bone and its tissue is given.

Bone is a two-phase porous natural composite material comprised primarily of collagen and mineral, which together provide its mechanical properties. The organic component, mainly collagen, gives bone its form and contributes to its ability to resist tension, while mineral component, inorganic, primarily resists compression. Bones are biological structural materials made of dynamically adaptable tissue. Its remodeling is described by *Wolf's law* (Wolff (1986)).

Although bones are similar in structure and development, they vary considerably in size and shape. The architecture of bones is composed of very complex material with extraordinary properties that optimally adjust to external loads or self-replacing mechanisms. In order to understand these properties it is important to understand the mechanical properties of all bone's component phases and the structural relationships among them at the various levels of hierarchical structural organization (shown in Figure 1 from *et al.* (1998).

Although all computations were carried on a microscale it was necessary to use results from other length scales (e.g. osteonal parameters from nanoscale, Lenz and Nackenhorst (2003)) in order to understand or describe mechanical and material properties. Figure 1 gives a good introduction into the hierarchical structure of a long bone.

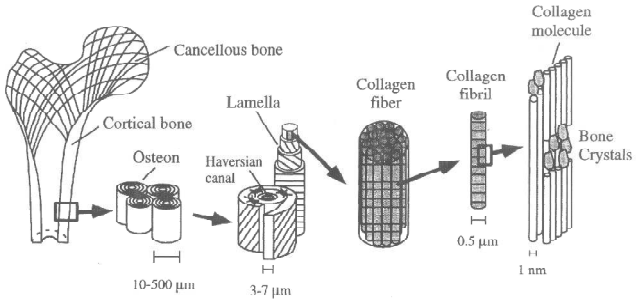

Figure 1: Hierarchical structure of bone tissue (Rho *et al.* (1998))

Figure 1 shows most commonly hierarchical levels appearing in a bone. The first one on the left side of the figure is called *macrostructure*; its main length scale is larger than 500μm and two bone types such as cortical and trabecular are determined. Next to the right *mesostructure* with length scale of 10-500 μm where single osteon, called also Haversian systems or single trabeculae, can be found. The center of the illustration presents *microstructure*. This is the most important scale in this work. Accordingly all presented models are built within microscale. With a length scale of 1 μm to 10 μm single osteonal lamellae can be determined. In length scale of a few hundred nanometers to 1 μm these lamellaes are structured of fibrillar collagen and embedded minerals which already pertain *nanostructure*. The last illustration on the right introduces the *subnanostructure*. With a length scale of some tens nanometers it is possible to observe molecular structure of the constituent elements such as hydroxyapatite crystals, collagen and non-collagenous organic proteins.

Figure 2 presents the typical long bone with its structure (Cowin (2001)). On the first sight two tissues can be distinguished which, among others, differ mostly in density. These tissues are called *cortical* and *trabecular*.

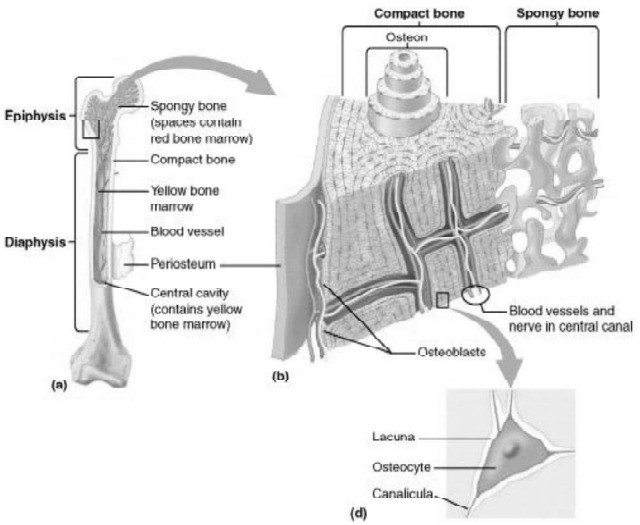

Figure 2: Illustration of bone structures- cortical (compact) and trabecular (spongy) found in Grass (2005)

3. MECHANOSENSITIVITY

The fact that bone tissue adapts its material properties, and the whole bone shape, in response to altered mechanical loading was proved and confirmed long time ago. However, the physiological mechanism by which the mechanical loading applied to the bone is sensed and the mechanism by which the sensed signal is transmitted to the cells has not been finally identified yet.

In order to make the theoretical description entirely complete, one more 'ingredient' ought to be presented – the *mechanosensation* process. Although the capacity of bone tissue to adapt to changing mechanical demands is well known, the reaction of bone cells is not fully understood. In the last decades significant progress has been made in understanding the bone cells reaction on mechanical signals, derived from bone loading. Lately, several theories concerning this problem have been developed (Cowin (1999), V. D. Meulen and Pren-dergast (2000), Turner and Pavalko (1998) or books like Cowin (2001), Martin *et al.* (1998)).

The *mechanosensation* process is responsible for detection of the mechanical loading on the bone. It is one of two main subprocesses of the *mechanotrasduction* (see below).

Mechanotransduction in Bone

bone loading

↓

matrix strain

↓

mechanosensation by bone cells

↓

intercellular signaling:
mobilization of BMU's
(basic multicellular units)

↓

bone remodeling

Mechanotransduction is the process which converts biophysical forces into cellular response and includes the cells reaction to the external loads.

The current theoretical and experimental evidence suggests that osteocytes (Cowin (2002)) are the principal mechanosensory cells of bone, which are activated by shear stress from fluid flowing through the canaliculi. The electrically coupled three-dimensional network of osteocytes and lining cells is the communication system for the control of bone structural strain detection. The described mechanosensory mechanisms in bone consist of:

1. The cell system that is stimulated by external mechanical loading applied to the bone,
2. The system that transduces that mechanical loading to a communicable signal,
3. The system that transmits that signal to the effector cells (osteoblasts, osteoclasts) for the maintenance of bone homeostasis and strain adaptation of the bone structure.

However, the way strains are detected in bones is still under research. After taking a closer look at bone, it becomes obvious that the network consisting of the above mentioned cells situated directly inside the bone tissue would have the capability to fulfill the demands of mechanosensation. At this point, it is necessary to adress the problem of strain detection in bone cells. Figure 3 shows the relationship between bone activity and strain detection. As presented there are two characteristic points MES_C and MES_R which are boundary values, according to which the remodeling processes of bone (resorption, creation) are carried out. These two values point out the so called *dead zone*, in which no change in bone occurs.

However, the problem is much more complicated than shown in Figure 3. Quantitative studying of the strain in bones of performing animals (galloping horses, fast-flying birds, even a running human volunteer) found a maximal strain not higher than 0.2% to 0.3% (Rubin (1984), Burr *et al.* (1996). This poses the problem in interpreting the results of *in vitro* studies of strained bone cells, where much higher deformations, 1% to 10%, are needed to obtain a cellular response (Murray and Rushton (1990), Burger and Veldhuijzen (1993)). According to Neidlinger-Wilke *et al.* (1995) 1% of unidirectional cell stretching is required to receive the response in cultures of human bone cells. However, in an animal study using rats, 0.15% bending strain of the intact tibia was already sufficient to activate cell proliferation and bone formation *in vivo* (Turner *et al.* (1994), Forwood (1996)). Assuming the strain to be somehow involved in bone cell mechanosensing means that bone tissue must possess a lever system whereby the small matrix strains are transduced into a larger signal that is sensed by bone cells.

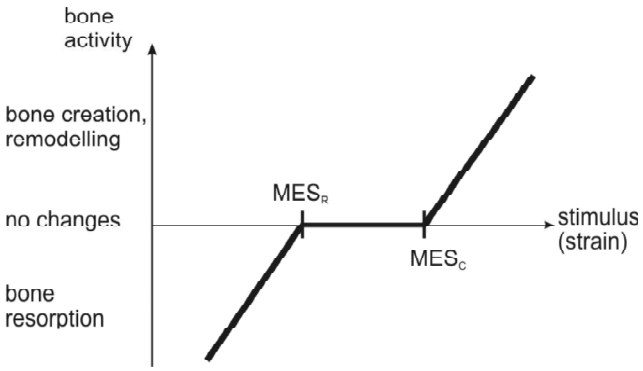

Figure 3: Relationship between the strain detection on the osteon and bone reaction

4. PURE STRAIN CONCEPT

The core of this concept is a reaction of osteocytes to pure strains or bone matrix deformations. The external forces act on the whole bone, and the strains caused on the macro length scale are the same as on the micro length scale of the osteocytes. But this problem is much more complex than described above. Several biological experiments were carried out and it was found that the strain occurring in osteocytes must be significantly above (about two orders magnitude higher) the strain expected in the bone (You *et al.* (2000), Burger and Veldhuijzen (1993)). According to other experiments strain values of about 1000 microstrain[1] is required in order to get a response from osteoblasts (Kaspar *et al.* (2000)) while Frost (1992) described that minimum as 1500 microstrain. With the strains of this magnitude bone will undergo remodeling and increase its density in order to reduce local strains. This action will last as long as the local strains are small enough. However, higher local strains will not cause any action and too high strains will cause damage in the bone tissue. There are two interesting models suggested. One of them is trying to explain how the osteocytes could amplify the strain to a level which would be detected by cellular mechanisms (You *et al.* (2001)) while the second attempts to clarify the problem of the *dead zone* (Rubin *et al.* (2002)). In this work the second model (see Figure 4) will be presented where osteocytes undergo even higher strains.

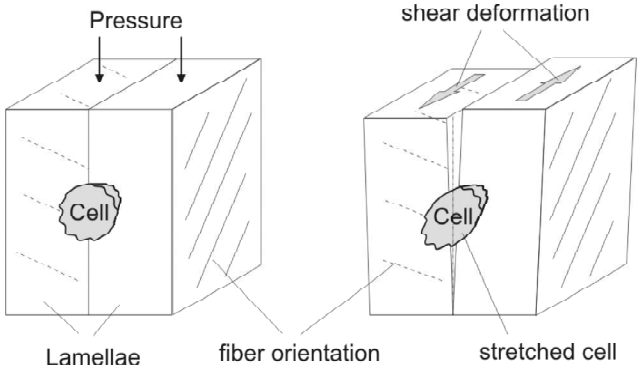

Figure 4: Osteocyte between two lamella with additional shear deformation

As shown in Figure 4 the model of two lamellae with different fiber orientation is presented with inbetween located osteocyte. The axial pressure, loading top surfaces of lamellae, causes additionally stretching strain, which is clearly higher in osteocyte localization than inside the lamellae. There is no evidence that these shear strains will be able to amplify the cell strains significantly enough. Fulfilling the models mentioned above and causing strain detection by osteocytes as a final effect seems however, quite probable.

It is generally accepted that continuum bone matrix strains are found to be in the order of 0.3 and 2 microstrains. Therefore, the minimum effective strains for numerical models presented in this work will be determined after the values given by Frost (1992).

5. FLUID FLOW HYPOTHESIS

The fluid flow is induced by dynamical external loads which cause a local hydrostatic pressure gradient. A hypothesis concerning the mechanism by which the osteocytes placed in the lacunae of mechanically loaded bone sense the load applied to the bone by the detection of strains was suggested by several researchers (Duncan and Turner (1995), Burger and Klein-Nulend (1999b), Burger and Klein-Nulend (1999a)). It was proposed that the osteocytes are stimulated by relatively small fluid shear stresses acting on the membranes of their osteocytic processes. The fluid flow is induced by dynamical external loads which cause a local hydrostatic pressure (see Figure 5).

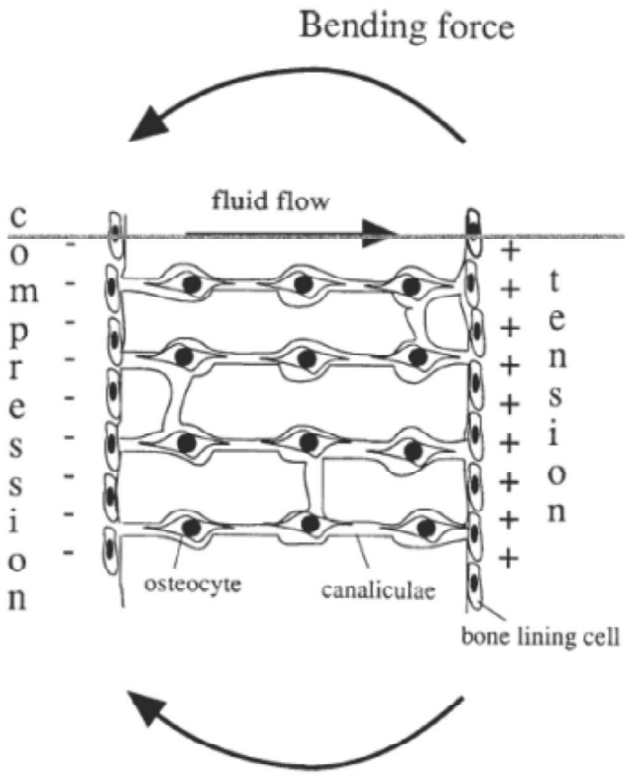

Figure 5: Creation of fluid flow through the hydrostatic pressure gradients

As presented on Figure 5 the bending forces not only deform the osteocytes situated inside the bone, but further generate a pressure gradient from compression to tension regions (Duncan and Turner (1995)). This causes the bone fluid to flow through the canalicular spaces, and in addition to causing shear stresses on cell membranes it also provides the cell with nutrien supplies. Additionally, a very characteristic electric potential is created which is called *streaming potential* and was introduced by

Korenstein *et al.* (1984). It is known that extracellular bone matrix is negatively charged due to its proteins. When the fluid moves, the excess positive charge is convected developing streaming currents. The amount of electrical current created is dependent on the pore sizes through which the fluid is pressed. The anatomical site in bone tissue that is the source of the experimentally observed strain generated potentials is still under discussion (Pollack and Petrov (1984)).

Although numerous experiments were carried out by Burger and Klein-Nulend (1999b), Owan *et al.* (1997), Wang *et al.* (2003) it is not finally proven if the mechanosensation process can be explained with the fluid flow theory.

6. CONTINUUM MECHANICS

The specific objects represent different outlook when seen with the naked eye and under a microscope. Material which appears to be continuum is not the same in a finer length scale. However, in *continuum theory* the fact that matter is made of atoms and that has some sort of heterogeneous microstructure is ignored in the simplifying approximation and physical quantities, such as energy and momentum, can be handled in the infinitesimal limit. Differential equations can thus be employed in solving problems in *continuum mechanics*. Some of these differential equations are specific to the materials being investigated, while others capture fundamental physical laws, such as conservation of mass or conservation of momentum (Zienkiewicz and Taylor (1994), Altenbach and Altenbach (1994), Betten (1993), and Wriggers (2001)).

The kinematic basics of continuum mechanics contain the description of solid body deformations, distortions and time derivation of the kinematic variables.

Formally, a solid body **B** can be described as an assembly of points in an EUCLIDIAN space ***E***. The configuration of **B** is the explicit transformation of $\varphi : B \rightarrow \mathbf{E}$ where the particle of **B** is included in ***E***. Therefore, the location of particle **X** of body **B** in configuration $\varphi(B)$ (coupling operator) is defined as $x = \varphi(X)$. Figure 6 (based on illustration in Wriggers (2001)) shows configurations: on the left *undeformed* called also *reference* (*B*) and on the right *deformed* or *actual* φ(B). As stated earlier, both configurations are coupled by the operator φ.

According to Figure 6 a particle **A** is situated in both configurations: reference **B** and actual $\varphi(B)$ but at different locations, respectively **X** and **x**. The location of particle **A** in time space $t \in R^+$ is described as follows:

$$x = \varphi(X, t) \tag{1}$$

The deformation of body **B** causes the displacement of particle **A** which is given by Equation 2:

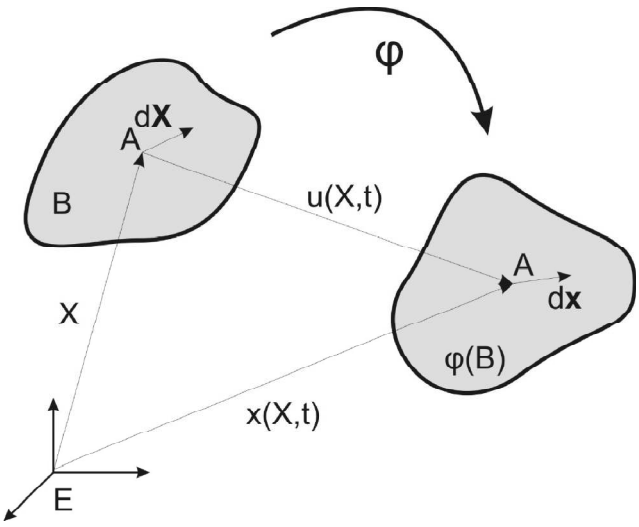

Figure 6: Motion, deformation of the body B

$$u(\mathbf{X}, t) = \mathbf{x}(\mathbf{X}, t) - \mathbf{X} \tag{2}$$

To describe deformation processes it is crucial to introduce the *deformation gradient* **F** which combines the deformation of the line element d**X** in reference configuration **B** with the deformation in actual configuration. This relation is given as:

$$d\mathbf{x} = Fd\mathbf{X} \tag{3}$$

Using partial derivatives the deformation gradient can be expressed as:

$$\mathbf{F} = \frac{\partial \mathbf{x}}{\partial \mathbf{X}} = \frac{\partial \mathbf{X}}{\partial \mathbf{X}} + \frac{\partial \mathbf{u}}{\partial \mathbf{X}} = 1 + Grad\mathbf{u} = 1 + \mathbf{H} \tag{4}$$

where $Grad\mathbf{u} = \mathbf{H}$ and is defined as *the displacement gradient tensor*.

If the deformation gradient operator is linear, the transformation given by Equation 3 is also linear. In order to provide the continuum structure of **B** during the deformation, Equation 3 must be unique.

$$J = det\mathbf{F} \neq 0 \tag{5}$$

where J is the Jacobian determinant. When the deformation gradient **F** is not singular there exists the inverse $\mathbf{F}^{-1}$ and Equation 2 can be written as follows

$$d\mathbf{X} = \mathbf{F}^{-1}\, d\mathbf{x} \tag{6}$$

The Jacobian determinant is of a great importance in continuum mechanics and the corresponding numerical formulation. It relates infinitesimal small volume elements such that

$$dv = JdV \tag{7}$$

Deformation gradients can be decomposed into stretch and rotation tensors using the *polar decomposition theorem* as follows:

$$\mathbf{F} = \mathbf{RU} = \mathbf{VR} \tag{8}$$

where respectively **R** is *the orthogonal rotation* tensor, **U** is *the right stretch* tensor and **V** is *the left stretch* tensor with

$$\mathbf{R}^T\mathbf{R} = 1\ \mathbf{U}^2 = \mathbf{F}^T\mathbf{F} = \mathbf{C}\ \mathbf{V}^2 = \mathbf{F}\mathbf{F}^T = \mathbf{b} \tag{9}$$

where **C** is described as the right and **b** as the left CAUCHY-GREEN tensor.

After describing the deformation gradient tensor **F** the GREEN-LAGRANGE strain tensor can be introduced as follows:

$$\mathbf{E} := \frac{1}{2}(\mathbf{F}^T\mathbf{F} - 1) = \frac{1}{2}(\mathbf{C} - 1) \tag{10}$$

The deformation gradient contains all information about displacement and rotation of the body. It is convenient to describe the GREEN-LAGRANGE tensor with use of the displacement gradient **H** (Equation 4) that gives

$$\mathbf{E} = \frac{1}{2}(\underbrace{\mathbf{H} + \mathbf{H}^T}_{linear} + \underbrace{\mathbf{H}^T\mathbf{H}}_{nonlinear}) \tag{11}$$

where the linear and non linear parts can be distinguished. In this work (except for one example) the linear theory will be used. The non linear part can be omitted which results in the linear strain tensor

$$\varepsilon = \frac{1}{2}(\mathbf{H} + \mathbf{H}^T). \tag{12}$$

With the use of the transport equation and the rule of mass conservation it is possible to derive the following expression:

$$\int_B \rho\dot{\mathbf{v}}dv = \int_B (div\sigma + \rho\mathbf{b})dv \tag{13}$$

In Equation (13) σ is the CAUCHY stress tensor and $\rho\dot{\mathbf{v}}$ represents the inertia which can be neglected in static mechanical problems. This leads to Equation (14)

$$\int_B (div\sigma + \rho\mathbf{b})dv = 0 \tag{14}$$

To solve for Equation (14) in the field of numerical methods it is necessary to introduce the variational formulation. The computation can be obtained with the use of the principle of virtual displacement, which multiplies Equation (14) with a test function η. The resulting expression is integrated over volume *B* and finally one obtains the following expression:

$$\int_B (div\sigma + \rho\mathbf{b})\eta dv = 0 \tag{15}$$

The final form of the weak formulation is as follows:

$$\int_B \delta\varepsilon^T\mathbf{C}\,\varepsilon dv - \int_B \delta\mathbf{u}^T\rho\mathbf{b}dv - \int_{\partial B_t} \delta\mathbf{u}^T\mathbf{t}da = 0 \tag{16}$$

where $\sigma = \mathbf{C}\cdot\varepsilon$, u is the unknown displacement and ∂B_t is the surface where **t** is applied.

The constitutive relation between the applied stresses and strains for linear materials at small strains is given by:

$$\sigma_{ij} = C_{ijkl}\varepsilon_{kl} \tag{17}$$

where C_{ijkl} represents the fourth rank material tensor (81 components). However on the basis of symmetry of strain (Equation 18) and stress (Equation 19) tensor it is possible to reduce the number of components to 36.

$$\sigma^T = [\sigma_{11}\ \sigma_{22}\ \sigma_{33}\ \sigma_{12}\ \sigma_{23}\ \sigma_{31}] \tag{18}$$

$$\varepsilon^T = [\varepsilon_{11}\ \varepsilon_{22}\ \varepsilon_{33}\ \varepsilon_{12}\ \varepsilon_{23}\ \varepsilon_{31}] \tag{19}$$

In this work the used materials are described below. Hydroxyapatite crystal, collagen matrix and osteocyte are isotropic linear elastic materials. With the use of only two independent constants, POISSON ratio ν and YOUNG modulus *E*, typical for engineering problems, it is possible to build the whole material matrix **C** as shown in Equation (20):

$$\begin{bmatrix}\sigma_{11}\\ \sigma_{22}\\ \sigma_{33}\\ \sigma_{12}\\ \sigma_{23}\\ \sigma_{33}\end{bmatrix} = \frac{E}{(1+\nu)(1-2\nu)}\begin{bmatrix}(1-\nu) & \nu & \nu & 0 & 0 & 0\\ \nu & (1-\nu) & \nu & 0 & 0 & 0\\ \nu & \nu & (1-\nu) & 0 & 0 & 0\\ 0 & 0 & 0 & \frac{(1-2\nu)}{2} & 0 & 0\\ 0 & 0 & 0 & 0 & \frac{(1-2\nu)}{2} & 0\\ 0 & 0 & 0 & 0 & 0 & \frac{(1-2\nu)}{2}\end{bmatrix}\begin{bmatrix}\varepsilon_{11}\\ \varepsilon_{22}\\ \varepsilon_{33}\\ 2\varepsilon_{12}\\ 2\varepsilon_{23}\\ 2\varepsilon_{31}\end{bmatrix} \tag{20}$$

Transversely isotropic material with anisotropic behavior is very specific for fiber composites in which it is possible to identify an orthotropic structure of the material. The typical structure of this unilateral composite and its orthogonal coordinate set which defines the orientation of the fibers is presented in Figure 7. The elastic constitutive relation for this material are than expresses as follows:

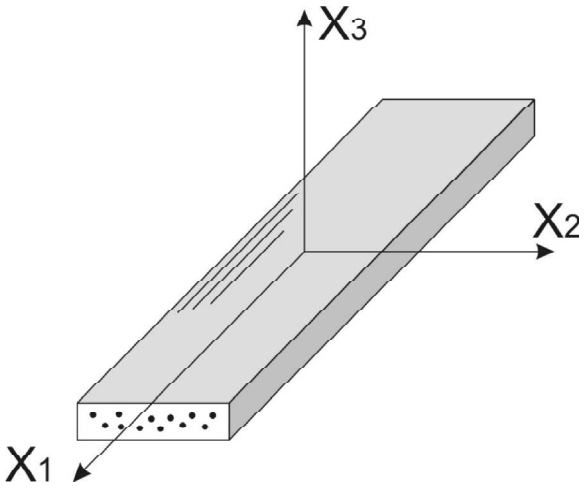

Figure 7: Definition of the coordinate axes with respect to the material symmetry axes

$$\begin{bmatrix}\sigma_{11}\\ \sigma_{22}\\ \sigma_{33}\\ \sigma_{12}\\ \sigma_{23}\\ \sigma_{31}\end{bmatrix} = \begin{bmatrix} c_{11} & c_{12} & c_{13} & 0 & 0 & 0\\ c_{12} & c_{11} & c_{13} & 0 & 0 & 0\\ c_{13} & c_{13} & c_{33} & 0 & 0 & 0\\ 0 & 0 & 0 & c_{44} & 0 & 0\\ 0 & 0 & 0 & 0 & c_{44} & 0\\ 0 & 0 & 0 & 0 & 0 & c_{66}\end{bmatrix} \begin{bmatrix}\varepsilon_{11}\\ \varepsilon_{22}\\ \varepsilon_{33}\\ 2\varepsilon_{12}\\ 2\varepsilon_{23}\\ 2\varepsilon_{31}\end{bmatrix} \quad (21)$$

where:

$$c_{11} = \frac{1-\nu_{31}^2\frac{E_1}{E_3}}{\Delta} \quad c_{12} = \frac{\nu_{21}+\nu_{31}^2\frac{E_1}{E_3}}{\Delta} \quad c_{13} = \frac{(1+\nu_{21})\nu_{31}}{\Delta}$$

$$c_{33} = \frac{(1-\nu_{21})E_3}{1-\nu_{21}-2\nu_{13}\nu_{31}} \quad c_{44} = \mu_{13} \quad c_{66} = \mu_{12} = \frac{E_1}{2(1+\nu_{21})} \quad (22)$$

with $$\Delta = \frac{1+\nu_{21}}{E_1}\left[1-\nu_{21}-2\nu_{31}^2\frac{E_1}{E_3}\right]. \quad (23)$$

7. HOMOGENIZATION

The constitutive material relations shown in this work have been derived under the assumption that the material parameters are homogenous in the entire body B. For heterogenous materials, e.g. composite materials, the constitutive equations are applicable only to homogeneous volume fractions. In these cases the homogenization procedures are used to create effective, homogenous materials out of heterogeneous composites. The effective material properties strongly depend on the elastic properties, the volume fraction, the orientation and dimension of the constituents on the micro level. In case of biological materials of small size, experiments to derive the material properties are very difficult to carry out. Analytical or numerical estimations of homogenized material parameters are sometimes useful alternatives, but they remain approximations. Having knowledge about the mechanical properties on the nano scale of the material constituents, effective material parameters can be derived for micro scale calculations. Therefore several homogenization procedures are described in the literature. They all have to fulfill certain requirements concerning RVE's (*representative volume element*). It has to be small enough on the computation scale, but large enough on the scale, where its properties are known. It can than be considered statistically representative.

One of the most widely used classical homogenization methods is the Mori & Tanaka (1973) method. It was used by Lenz and Nackenhorst (2003) to obtain nano parameters of the bone on the micro scale.

This method is an extended approach to homogenization considering the interaction between the inclusions and their finite volume fraction. Therefore, the strain field of the matrix is approximated through the average strain field in a sufficient distance. The load on each inclusion depends on the existence of other inclusions and the average matrix strain and stress fields created by them. The interaction does not include the fluctuation of the fields. Finally, the effective material **C*** is calculated by:

$$\mathbf{C}^* = \mathbf{C}_M + c_I \cdot (\mathbf{C}_I - \mathbf{C}_M) : \mathbf{L}_{MT} \quad (24)$$

where $\mathbf{C}_M$ and $\mathbf{C}_I$ are the fourth order material tensors of matrix and inclusion, respectively. The parameter c_I is the concentration of inclusion and $\mathbf{L}_{TM}$ is the localization tensor based on the Mori & Tanaka assumption

$$\mathbf{L}_{MT} = [\mathbf{I} + c_M \mathbf{S}_M : (\mathbf{C}_M^{-1} : \mathbf{C}_I - \mathbf{I})]^{-1}. \quad (25)$$

The localization tensor represents the solution of a linear elastic boundary value problem of the following form

$$\varepsilon_{ij}^I(x) = L_{ijkl}(x) : \varepsilon_{kl}^0 \quad for\ u_i = \varepsilon_{ij}^0 x_j \quad on\ \partial\Omega, \quad (26)$$

which means that if the strain ε° in the matrix material acting on the boundary of the inclusion $\partial\Omega$ is known (assumed to be constant in this case) then the calculation of the strain field ε^I inside the inclusion becomes possible.

The localization tensor itself depends on both material tensors, the matrix concentration and the fourth order ESHELBY tensor **S** (Eshelby (1957)). The ESHELBY solution denotes that inside ellipsoidal inclusions, if the strain field ε^t is constant, the resulting total strain field ε^t is also constant. These two strain fields are coupled by the fourth rank ESHELBY tensor **S**:

$$\varepsilon_{ij} = S_{ijkl} : \varepsilon_{kl}^t = const\ in\ \Omega \quad (27)$$

In the case of simple inclusion geometries, analytical solutions for the ESHELBY tensor are known and may be denoted explicitly. In other cases, numerical approximations of this tensor have to be computed.

8. MATERIAL MODEL

The mechanical behavior of osteons depends on their elastic properties which are essential and must be determined to carry out the finite element analysis. Thereby many factors play a role like the fiber pattern of the lamella, the degree of mineralization as well as the elastic properties of the main constituents of bone tissue: HA-crystals and collagen molecules. Taking into consideration the scale in which this research was done the dimensions of osteon and the dimensions of HA-crystals (2x4x20nm), homogenization methods become necessary. The homogenization allows the creation of a material which has the same elastic properties as a composite of HA-crystals and collagen as shown in Figure 8:

Another important fact of the osteon material belongs to its anisotropy. This anisotropy arises basically from the approximately ellipsoidal (also cuboidal according to other researchers) HA-crystal structure. Despite of the isotropy of collagen and hydroxyapatite, the homogenization yields an orthotropic lamella material. Thus, three principle axis for the stiffness of the lamella material are obtained where the highest stiffness belongs to the semi-major axis of the ellipsoid.

For homogenization the classical MORI-TANAKA method is used and the following elastic properties of the components are applied as shown in Table 1:

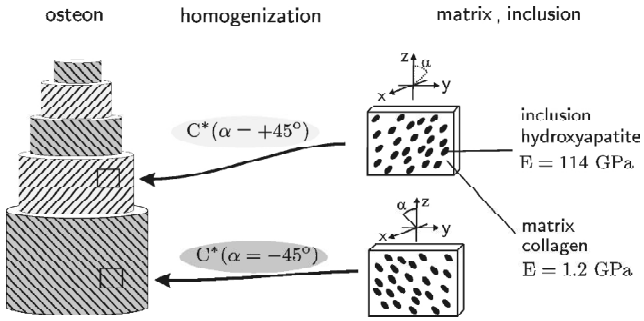

Figure 8: Structure of the Haversian System (Osteon)

Table 1
Elastic Properties of Collagen, HA and Composite Created after Homogenization

Material	*Young's modulus*	*Poisson's ratio*	*Symmetry*
collagen	1.2GPa	0.35	isotropic
hydroxyapatite	144GPa	0.27	isotropic
composite	5-18GPa	0.3	orthotropic

The big dispersion of the composite material stiffness is strongly connected with the concentration of ellipsoidal HA (mineralization) in the RVE. The problem is addressed in the following section below.

For the process of homogenization, the HA- crystals are called inclusions (particles) and the collagen is referred to as matrix. With the use of the MORI-TANAKA method, it is possible to calculate the material matrix **C*** of the composite material (lamella material).

Finally, the lamella material **C*** has to be rotated in the directions in which they appear in the osteon. Here the example of lamellae ±45° (see also Figure 8) is introduced:

$$C_{ijkl}^{45^\circ} = C_{mnop}^{*} D_{lp}(45^\circ) D_{ko}(45^\circ) D_{jn}(45^\circ) D_{im}(45^\circ). \qquad (28)$$

where **D(α)** is the rotation matrix around 1-axis of *alpha* degrees:

$$\mathbf{D}(\alpha) = \begin{pmatrix} 1 & 0 & 0 \\ 1 & \cos(\alpha) & -\sin(\alpha) \\ 1 & \sin(\alpha) & \cos(\alpha) \end{pmatrix} \qquad (29)$$

After the execution of all steps, including the rotation procedure, the orthogonal material tensor can be obtained.

1. Geometry of the Model

To solve the mechanical problem of an ordinary osteon under physiological boundary conditions a three dimensional finite element model is developed. The geometry of such a model is idealized to a simple hollow cylinder, and further, with the use of periodical boundary conditions, simplified to 60° section (see Figure 9 on the right and Figure 14).

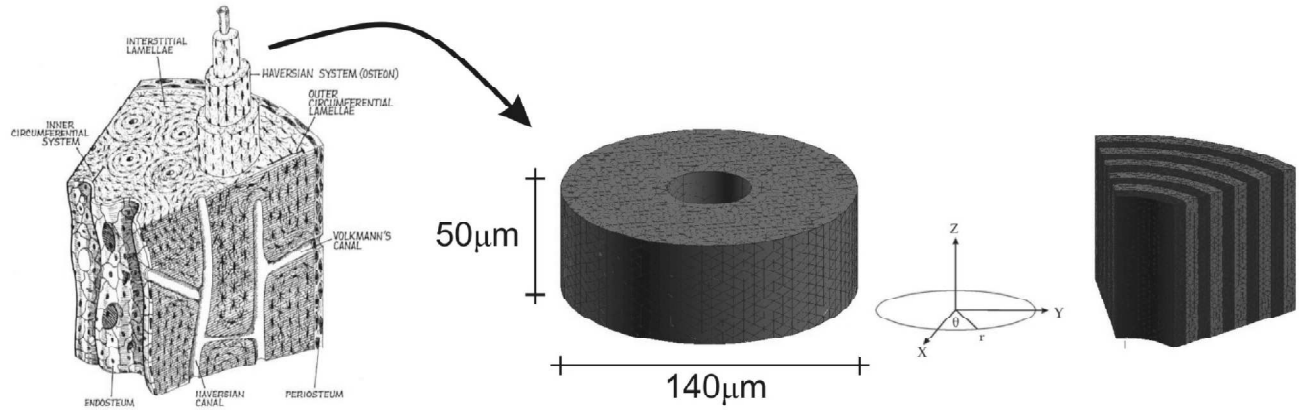

Figure 9: Part of Haversian system in the numerical approach

The modeling process in this work is carried out according to the theory presented earlier. All properties are defined in a cylindrical coordinate system (Figure 9) in order to obtain axial symmetry. The small osteon models presented in this work contain only two lamellae. Each of them has a radial width of 5 μm and a height of 50 μm. The radius of the inner hole is 40 μm.

There are several theories describing the geometry of osteocytes. According to COWIN (2001) they are spherically shaped with diameters of 4–14μ*m*. Martin

et al. (1998) suggested even smaller dimensions while Fritton *et al.* (2004) accept more specific shapes of a triaxial ellipsoid with axes lengths of $17.6 \pm 0.3\ \mu m$, $6.1 \pm 0.3\ \mu m$ and $4.0 \pm 0.2\ \mu m$. According to these data the osteocyte geometry was chosen and is presented below.

The geometry of the models prepared in previous research (e.g. Lenz and Nacken-Horst (2003)) poorly approximated the shape of the osteocyte which did not reflect the real biological geometry. Here, this geometry is substantially improved. It was decided to create two kinds of models one with spherical osteocytes with diameter of $5\mu m$ and the second one with ellipsoidal osteocytes with axial lengths of $2.5\mu m$, $2.5\mu m$ and height of $5\mu m$. That gives the opportunity to compare the differences arising during the computation process and present the geometrical development of the model. Models with both kind of inclusions are presented in Figure 10. The location of osteons (red on Figure 10) is random.

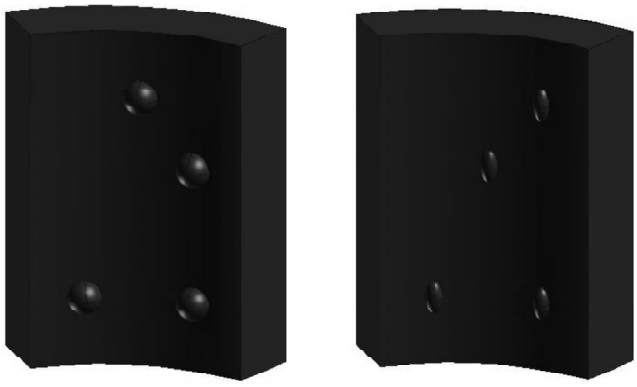

Figure 10: The lamella with spherical (left) and ellipsoidal (right) osteocytes

To make the geometrical description complete the number of osteocytes in the lamellar tissue must be discussed. Here arises another disaccord occurring in several sources. According to Cowin (2001) the number of lacunae per mm^3 is about 15000. Martin *et al.* (1998) supports this number, suggesting 13000-17000 lacunae per mm^3, but Fritton *et al.* (2004), who also suggested the largest axial sizes of the osteocyes, proposes much larger value of 80600 lacunae per mm^3. These relatively large differences confirm the lack of consensus in research. In order to hold one source geometrical data the number of osteocytes for the final model as well as the shape and size are those proposed by Cowin (2001) and Martin *et al*. (1998). However, for the small two lamellae models which should only describe the modeling approach these values are not applied. Here four osteocytes are placed between lamellar layers. At this point the model development is shown. The exactness of the biology representation is discussed later.

2. Material Properties

The created models in this research use great variety of the material properties (described earlier) but all of them are generated for the mineralization degree of 65%. All orthogonal material tensors used for the modeling in this research and describing the properties of the lamella with specific fiber orientation are expressed in VOIGT notation. The orthotropic tensors for the fiber orientation 0° and 90° look identical to transversal isotropic material matrices. The other material tensors look very similar. The differences lie in the rotation routine which causes the material axes not to coincide with the cartesian coordinate system axes. However, the obtained homogenized material behaves in transversal isotropic way which means that exchanging the x and z-axes would not affect the material properties.

According to the biological studies the osteocytes are modeled with much softer material than lamellae, as fully elasto–isotropic material, described with two material parameters YOUNG's moduli $E = 0.2GPa$ and POISSON ratio $\nu = 0.3$.

3. Model Discretization

For the discretization process the 10-node tetrahedral elements with quadratic shape functions are used to describe the geometry. The discretization is shown in Figure 11.

Figure 11: Discretization of lamella inclusion; spherical (left) and ellipsoidal (right)

The discretization is carried out in a very specific way. Except of big size differences between modeled elements (lamella layer and osteocyte) which is discussed later, the use of MPC (multi point constraint) boundary condition requires characteristic properties. Therefore the right side of the lamellae is discretized first with the two dimensional triangle elements. Next, these elements are copied to the opposite surfaces on the left, hence corresponding nodes are created. Thereafter, the entire net was created based on the already existing one. The obtained discretization fulfills the boundary conditions

requirements and additionally provides very good visualization of the results.

The sizes of osteocytes in comparison to the lamellar layers are relatively small. Although the discretization of the osteocytes must be fine to obtain satisfactory results, the size of the elements composing the lamellae layers cannot be the same. That would cause enormous number of elements and makes the computation difficult to carry. In Figure 12 the single discretization of the osteocytes placed in the lamella is shown.

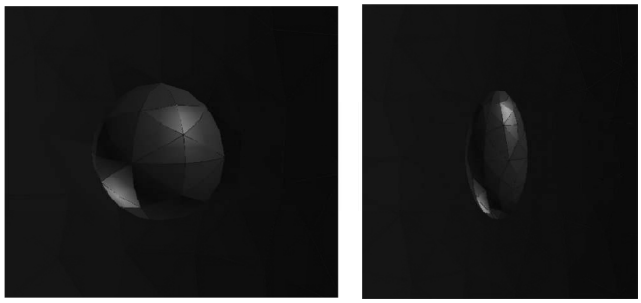

Figure 12: Illustration of the discretized osteocytes with surrounding lamella; spherical (left) and ellipsoidal (right)

The number of elements for the spherical osteocytes is smaller than the number of ellipsoidal osteocytes (as shown in Figure 12). This comes off the size differences–the smaller ellipsoidal inclusion requires finer discretization than the larger spherical ones.

The discretization has to provide the union between the lamellae layers and osteocytes placed between them. This could be proved by the continuities of the displacements and strains occuring in the osteocytes. By using the *nodal equivalence* function which eliminates double nodes in the model, the expected results are obtained in computation.

4. Boundary Conditions

There are two main boundary conditions applied to the generated model. The first one fixes the bottom of the model in the z-direction. The second, makes possible the reduction of the entire cylindrical osteon. In this work, only the section of 60° is modeled and computed (see Figure 13).

This reduction is possible due to *the periodical boundary conditions* which are applied at the side boundaries. This is realized by Multi Point Constraint (MPC), by which the same deformations in the section are obtained as if the whole osteons are analyzed. Periodical boundary conditions imply that the deformation of two, axial symmetric corresponding nodes (same radial distance to the center and the same z-dimensional hight at both sides) is equal. In order to obtain such a method the side surfaces (Figure 14) had

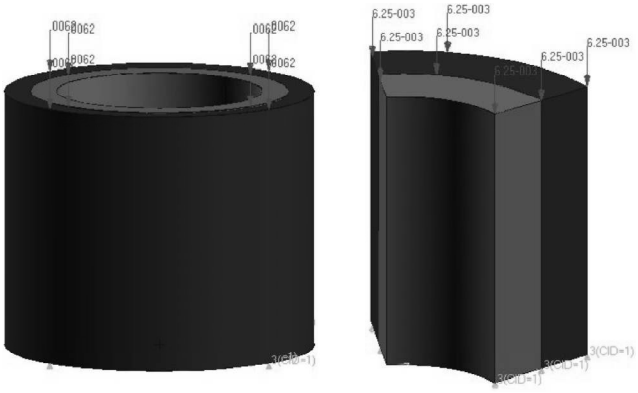

Figure 13: Entire cylinder of the osteonal model (left) and a section of 60° (right)

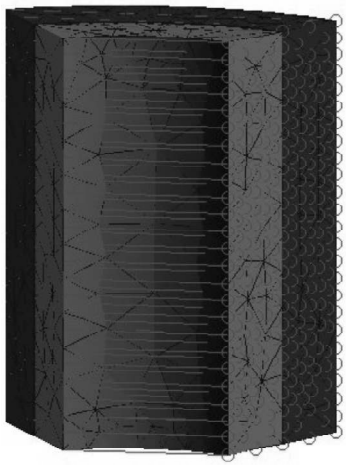

Figure 14: Periodical boundary conditions applied in the osteon model

to be discretized, one after another, with triangle surface elements that results in creation of the corresponding nodes.

The corresponding nodes are constrained with MPC. This tactic tremendously reduces the time and required memory of the computations. In Figure ??0 the MPC for a 2-lamellae osteon model is presented. The red circles show the node locations and the red lines connect two corresponding nodes.

5. Loading

On the top of the model a uniform physiological pressure of 6.25 *MPa* is applied. This value was estimated by Lenz (2005) according to the experimental and literature review – COWIN (2001), Martin *et al.* (1998) and others. The illustration of the loading application is shown on the right in Figure 13.

6. Results without MPC Boundary Conditions

In Figure 15 the displacements of the model without MPC boundary conditions is shown. The displacement distribution is similar for both cases. A very interesting behavior of the displacement can be noticed which relates

to the material parameters **C** and the fibriform structure with opposite fiber direction (±45°) for each lamella.

In Figure 16 the cross sectional view of the HUBER von MISES strains are presented.

This model is calculated with the use of all modeling methods described in this work excluding the MPC boundary condition. The HMH (Huber, Mises, Hencky) strains are calculated according to the equation $\varepsilon_{red} = \sqrt{\frac{3}{2}\varepsilon_{ij} \cdot \varepsilon_{ij}}$. The strains in osteocyte are clearly higher than those in the lamellae, which, according to the material parameters, is expected.

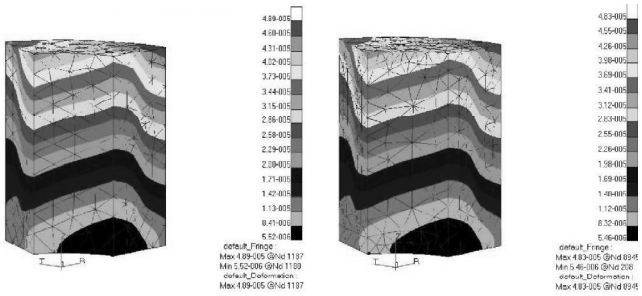

Figure 15: Total displacements of both models, left with sphere and right with elliptic osteocytes

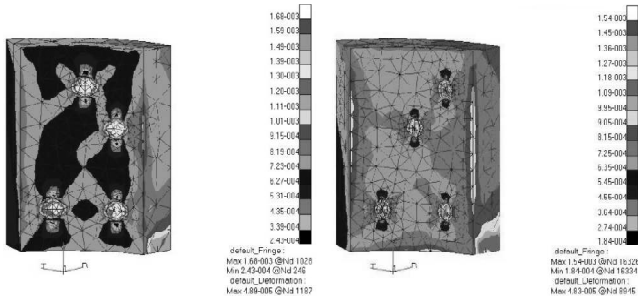

Figure 16: Cross-sectional view of MISES strains, left with sphere and right with elliptic osteocytes

The presentation of the displacement and strains showed that the model is created properly. The displacement of separately discretized lamellae are united and the strains occurring in softer osteocytes are higher than those obtained in the lamellar tissue.

7. Results with MPC Boundary Conditions

With the use of MPC boundary conditions, the displacements become symmetric as expected. They are presented in Figure 17. The cross-sectional strains are very similar to those presented in the previous section, and will not be shown again.

At this point one more very characteristic displacement property will be presented which is illustrated in Figure 18. As stated earlier, the periodical boundary conditions guarantee the same behavior of a section of 60° as if the whole cylindrical osteon would have been analyzed. It means that there should not be any possibility of displacement of the section's sides in the φ direction. With the use of a greater scale factor (0.1) and proper view it is possible to notice the displacement differences between models with and without MPC. They are compared in Figure 18.

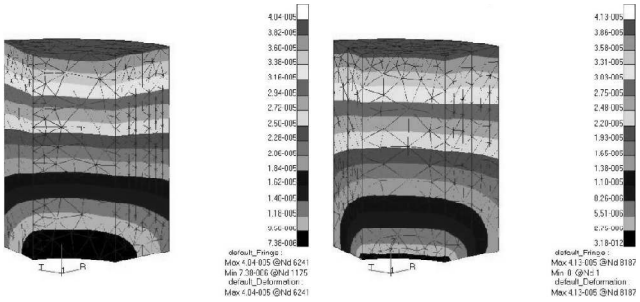

Figure 17: The displacement of osteon models with periodical boundary conditions, model with spherically shaped osteocytes on the left and with elliptically on the right

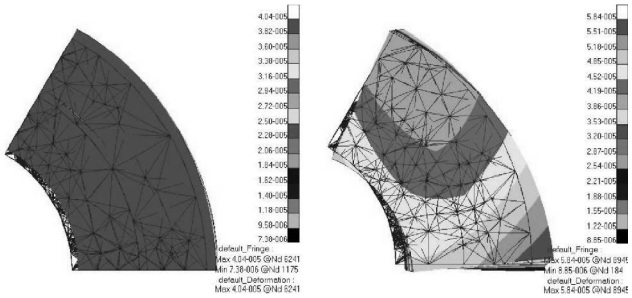

Figure 18: The model with MPC on the left, and without, on the right

The whole modeling procedure is presented and explained in this work. All the modeling requirements are fulfilled. With such an experience, creating the entire model is much easier and takes less effort. However, the computation time is longer because of the model size. In the the following section detailed description of the entire models with both kinds of osteocytes (spherical and ellipsoidal) will be given and obtained results will be compared with the theory developed earlier.

9. NUMERICAL EXAMPLES

The finite element analysis results of the osteon model with ten lamellae layers is presented in these examples. The aim is to study the deformations between the osteonal lamellae where the lacunae are situated. Each lacuna accommodates an osteocyte, and the strains at these locations are responsible for the initiation of the remodeling processes.

The full model description is given in Table 2.

Using the periodical boundary conditions, the entire cylindrical model is reduced to a section of 60°. It leads to the model shown in Figure 19. The number of osteocytes is obtained according to the information

presented earlier. Table 3 presents the calculation of the number of osteocytes for the model.

The location of the osteocytes is random and is chosen to be between 3rd and 4th, and 7th and 8th lamella. Both models with spherical and ellipsoidal osteocytes are shown in Figure 20.

Table 2
Parameters of the model (properties, boundary conditions and loading)

Model Parameters	
Diameter of entire ostenal cylinder	140μm
Diameter of inner whole (Haversian canal)	40μm
Hight of the entire model	50μm
Number of lamellae	10
Radial width of single lamellae	5μm
High of single lamellae	50μm
Diameter of the spherical osteocytes	5μm
Axial dimensions of the ellipsoidal osteocytes	2.5μm, 2.5μm and 5 μm
Botton boundary conditions	z-fixed
Side boundary conditions	MPC
Loading top surface pressure	6.25 MPa

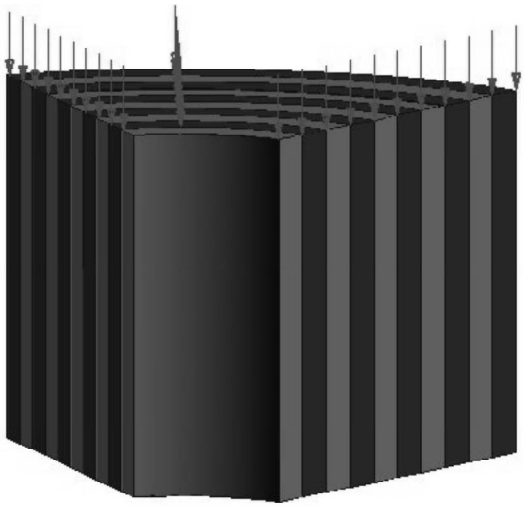

Figure 19: Geometry and loading pressure of the entire osteon model

The geometry, boundary condition and loading are now determined and the model is almost ready for the simulation. The computation of both models, as presented in Table 5, is carried out with different lamellae material parameters. Six different models are created, three with spherical and three with elliptical osteocytes. For all simulations the hydroxyapatite concentration (degree of mineralization) was set to 65%, which describes fully mineralized osteons.

The orientation of collagen fibers between lamellae may change up to 90° in adjacent lamellae. Except of orthogonal models, where the collagen fibrils only assume one of two directions which are out of phase 90° with each other, there is also the possibility of a twisted model. In this case parallel collagen fibrils continuously rotate by a constant angle from plane to plane in a concentric structure. In this work, three most common lamellae fibril orientations are simulated. The first group of two models with spherical and ellipsoidal inclusions, has the angles of fiber inclination for a cross ply lamellae pattern of ±45°, in the second, the angles are respectively 0° and 90° and the third group is an example of the twisted model, where the angle of fiber inclination is rising from –45° to 90° with 15° increase between each lamellae. The summary of the all models with different material properties is given in Table 4.

The geometry of both models with different shapes of osteocytes was presented before. Discretization and setting the boundary condition with use of MPC was carried out in the same way as it was presented for the small model in the previous sections.

Table 3
Number of osteocytes in a model

Calculation of number of osteocytes	
Volume of all cylindrical model including Haversian canal	0.000769mm^3
Volume of Haversian canal	0.0000628mm^3
Volume of all cylindrical model without Haversian canal	0.000706mm^3
Volume of 60° section	0.000117mm^3
Number of lacunae (Cowin (2001), Martin et al. (1998))	15000-17000/mm^3
Number of lacunae for the final model (60° section)	$1.7 – 2.01 \approx 2$

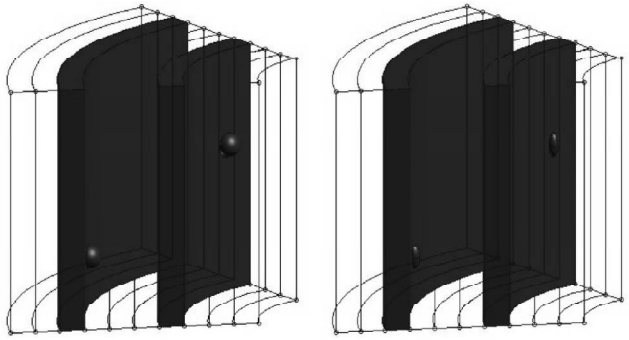

Figure 20: The entire model geometry with the location of spherical (left) and ellipsoidal (right) osteocytes

However, between the two models presented in Figure 20 there are some discretization differences. This arises due to the fact that the geometry of the inside inclusions is not the same. Smaller ellipsoidal osteocytes require finer tetrahedral elements than the larger spherical ones. The differences of the discretization data are shown in Table 5.

The FEM models with both kinds of osteocytes look identical. Though their surfaces are discretized in the exactly same way to obtain the corresponding nodes and MPC so that there is no visual differences in the external view. The entire discretized model is presented in Figure 21.

The finite element model, presented in Figure 21 is generated in MSC.PATRAN Simulating Reality software. After creating the model, an input file is produced. ABAQUS is used to solve the linear elastic mechanical problem. There is also one nonlinear computation carried out for the model with spherical inclusions and ±45° fibers orientation. It is presented and compared with linear calculations. According to different model parameters, which are the shape of inclusions and material parameters, the displacements at nodal points are calculated. Next, strains and stresses are obtained. These results are presented in the following Sections.

1. Model Including Lamellae with ±45° Fiber Orientation

In Figure 22 the displacements of models with different inclusions are shown in *millimeters*. On the left, the model with spherical osteocytes and, on the right, with the ellipsoidal osteocytes. The displacement distribution for both models is very similar and does not differ significantly from each other. Due the to periodical boundary conditions the problem is symmetrical. The largest displacements are on the top for both models, and they get smaller in the lower portion. These values vary between $4.31 \cdot 10^{-2}$ and $0.884 \cdot 10^{-2}$ micrometers for model with spherical inclusions, and $4.29 \cdot 10^{-2}$ and $0.935 \cdot 10^{-2}$ micrometers for model with ellipsoidal inclusions. The displacements on the top of the models are nearly constant while in the lower region they get larger with increasing radius. It is visible in Figure 22 that the shape of the osteocytes do not have significant influence on the displacement distribution and values.

Additionally, the computations of the the model with spherical inclusions is carried out with the nonlinear theory to compare the plausible differences to the linear elastic computation. The displacement field is shown in Figure 23. The non linear computation did not show any differences in displacement field distribution as well as in displacement values in comparison to the linear computations of the same model. Both results are quasi identical (Figure 22 on the left for linear and Figure 23 for nonlinear computation).

The strains presented in Figures 24 and 25 are essential for this work, especially the values at the lacuna locations where the osteocyte elements are placed. The strain in the osteonal corpus of the models are relatively constant therefore in Figures 24 and 25 only the two characteristic lamellar layers with the inclusions-4th and 8th lamella are presented.

Table 4
Material parameters (65% mineralization) for six osteonal models computed in this work

Kind of inclusion	*Fiber orientation*	*Description of appearance*
Model with spheres	±45°	lamella with smallest radius –45°
Model with spheres	0;90°	lamella with smallest radius 0°
Model with spheres	–45°/(+15°)/ + 90°	lamella with smallest radius –45°
Model with ellipses	±45°	lamella with smallest radius –45°
Model with ellipses	0;90°	lamella with smallest radius 0°
Model with ellipses	–45°/ +14° / + 90°	lamella with smallest radius –45°

Table 5
FEM data of the models with different inclusions

Number of nodes	160274	201862
Number of elements	109905	142806
Number of equations	480822	605586
Required memory for the calculation	3.04*G Bytes*	4.87*G Bytes*

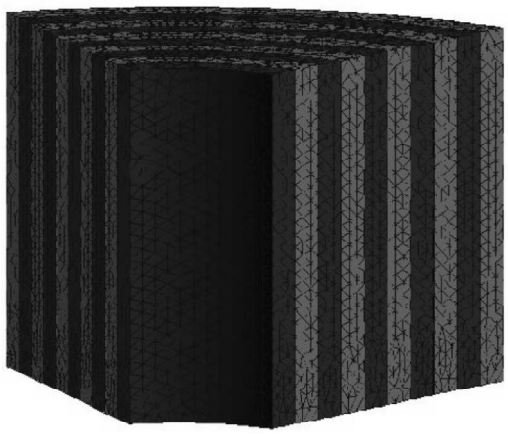

Figure 21: The view of discretized models with different types of inclusions

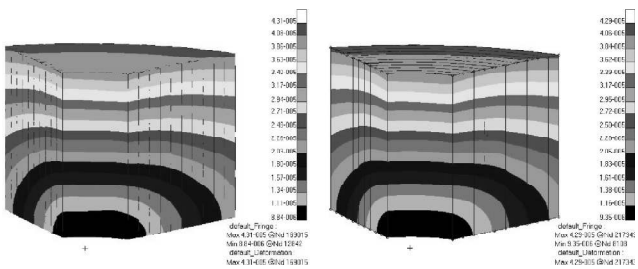

Figure 22: The model displacements after finite element analysis in *mm*. On the left the model with spherical inclusions, on the right with ellipsoidal inclusions

In Figure 24 both presented models contain spherical osteocytes. They are computed according to two different theories, the model on the left is calculated with linear analysis while the model on the right is calculated with nonlinear analysis. It is clearly visible that the results of these two different computational methods are almost identical. The reason lies in the resulting small strains, which makes the nonlinear analysis obsolete. Both models present exactly the same strain values and distribution. The strains in the lacunae are between $9.67 \cdot 10^{-4}$ and $1.65 \cdot 10^{-3}$ (red, yellow and pink colors) while the strains in the osteon corpus are much more constant from $5.79 \cdot 10^{-4}$ to $6.76 \cdot 10^{-4}$ (red and blue colors). For the entire osteon corpus the strains can be approximated with about 0.7 millistrains while at the lacunae the maximum value of 1.65 millistrains is located. These comparatively higher strains at the lacuna results from the lower stiffness of the osteocytes elements. The main contribution to the total strain derives from the longitudinal ε_z strain component which has nearly the same value as the total strain. The influence of all the other strain components is much smaller and remains lower than 0.5 millistrains.

In Figure 25 the obtained strains are presented; on the left the strains in the model with ellipsoidal inclusion and on the right the magnification of the strains in the osteocyte. As in the previous models, the osteocyte material is much softer than the osteonal corpus therefore the strains in the lacunae are three to four times higher. Their values vary between $1.15 \cdot 10^{-3}$ and $2.66 \cdot 10^{-3}$ (red, pink and green color) while the strains in the osteonal corpus present even more stable values (than for the spherical inclusions 24) of $6.44 - 8.12 \cdot 10^{-4}$ (constant blue color). The approximation of the strains in the model would result in 0.7 millistrains for the osteonal corpus. The maximal strains in the osteocytes is computed to be 2.66 millistrains. The main contribution to the total strain derives, as for the previous models, from the longitudinal (ε_z) strain component, while the other components remain much smaller (less than 0.4millistrains).

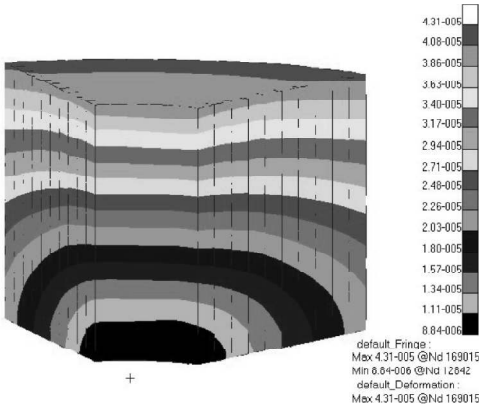

Figure 23: The displacements of model with spherical inclusion for non linear computation

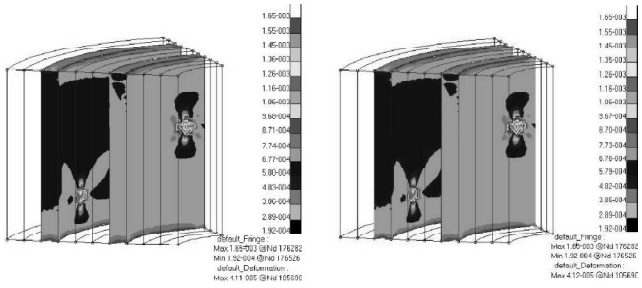

Figure 24: Strain distribution in osteon model. The model with spherical inclusions: on the left the results of the linear and on the right of nonlinear analysis

An additional characteristic property is now presented – the shear stress $\sigma_{\varphi z}$. The lamellae in both models (see Figure 26) changes the value in a very specific, alternating way (colors green and pink). For both examples the green color presents the shear stress $\sigma_{\varphi z}$ in lamellae as negative while the pink color presents the positive values. The reason for these results is the orientation pattern of the fibers in the lamellae which correlates to the main stiffness axes. These axes of the pink lamellae lie in the positive while the green lamellae lie in the negative circumferential direction.

The comparison of the presented strains for spherical and ellipsoidal inclusions shows that the strains in the osteonal corpus under specific pressure remains the same, 0.7 millistrains for both kind of models. Comparing these values with the simulation made by Lenz and Nackenhorst (2003) (their model was programmed in Matlab programming language) it turned out that the results in the osteonal corpus are very similar.

The strains obtained in the osteocytes vary significantly. The maximal value for the spherical inclusions is estimated to be 1.65 millistrains while for the ellipsoidal 2.66 millistrains. In comparison with the results presented by Lenz and Nackenhorst (2003), about 1.16 millistrains, both results obtained in this work are up to almost 1.5 times higher. The model by Lenz and Nackenhorst (2003) had the same material parameters, but much simpler geometry for the osteocytes (two hexagonal elements). These relatively high difference in strain detection, caused by the different geometry of the osteocytes, shows how important the modeling approach is, and might suggest and explain the most proper shape for the osteocytes.

The other conclusion concerns the nonlinear calculation, which takes much more time and requires, in comparison to the linear theory, much more memory to save the huge results data. There are no differences between the results obtained in linear elastic and nonlinear analysis. Therefore, the following computations will be carried out only according to the linear elastic theory which turns out satisfactory for this example.

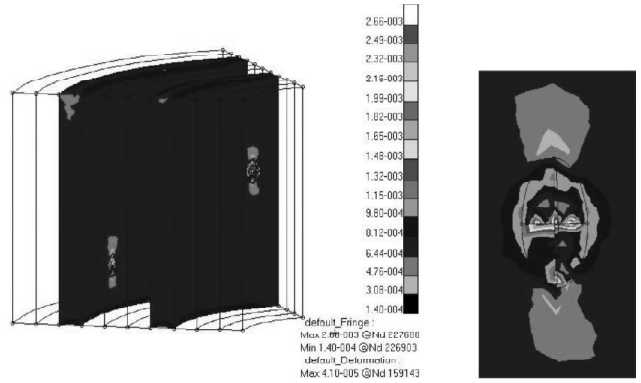

Figure 25: The strains in the model with the ellipsoidal inclusions (left) and the larger magnification of the strains in the osteocyte (right)

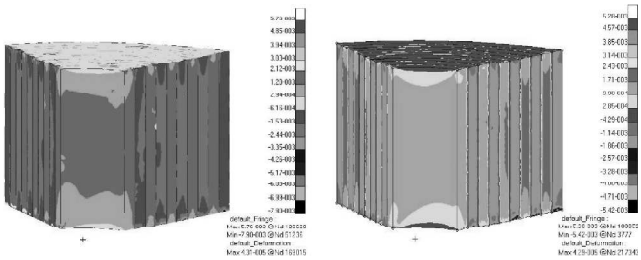

Figure 26: The shear stress $\sigma_{\varphi z}$ shows an interesting behavior. On the left model with spherical and on the right with ellipsoidal inclusions

2. Models Including Lamellae with 0° and 90° Fiber Orientation

Another osteonal model computed in this work (see Table 4) has the fiber orientation in a phase of 90° : 0° and 90° respectively. On Figure 27 the displacements of the models with spherical (left) and ellipsoidal (right) inclusions are presented.

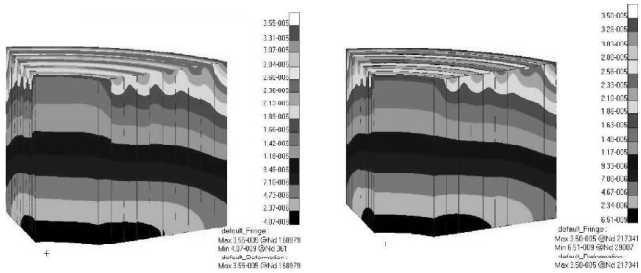

Figure 27: Displacement distributions, strongly dependent on the fiber orientation. A model with spherical (left) and with ellipsoidal (right) inclusions

Similar to the previous models the displacement values (in mm) and distribution for both cases are very similar that suggests that the shape of the inclusion does not influence the total displacement. This behavior, especially in the top region is noticeable. This property is strongly connected with material parameters. The 1^{st}, 3^{rd}, 5^{th}, 7^{th} and 9^{th} lamella have the fiber orientation of 0°. The fibers are situated exactly parallel to the loading direction, so their stiffness in this direction is the highest. Analogically the stiffness of fibers with orientation of 90° for such an axial loading is the smallest. It causes the entire lamella stiffness with fibers orientation of 0° to be much higher than the other lamellae. This explains the characteristic displacement, but also the strain distribution in the top region. In the middle part of both models the displacement fields are nearly constant, very similar to the previous example and in the lowest part they get larger with increasing radius however, not as much as those in the previous example. The displacement values in the top region are slightly higher than in the model with fibers orientation of ±45° but in the lower part they appear to be much smaller. For both models the displacement values are very similar and vary between $3.55 \cdot 10^{-2}$ and $4.07 \cdot 10^{-6}$ micrometers for the model with spherical inclusions and between $3.50 \cdot 10^{-2}$ and $6.51 \cdot 10^{-6}$ for the ellipsoidal inclusions.

In Figure 28 the strains in the models with both kinds of inclusions are presented.

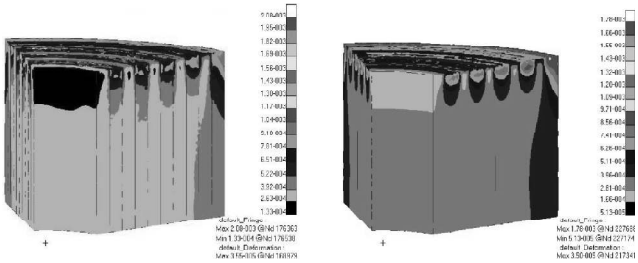

Figure 28: The strain fields of both models; with spherical (left) and ellipsoidal (right) inclusions

The distribution, as well as strain values for the osteonal corpus are qualitatively similar for both models. The above explained stiffness of lamellae with different fiber orientations (see displacement description) is the reason of the characteristic strain distribution in the top region of the models. The softer material under specific loading results in higher strains than the stiffer one. It is clearly visible especially in the 1^{st} and last lamella of both models. The strain values in the softer lamellae, the one with the fiber orientation of 90°, vary between $6.51 \cdot 10^{-4}$ and $9.10 \cdot 10^{-4}$ for the model with spherical inclusions and between $5.11 \cdot 10^{-4}$ and $9.71 \cdot 10^{-4}$ for the model with ellipsoidal inclusions. For the lamellae with higher stiffness (fiber orientation 0°) these values vary between $1.33 \cdot 10^{-4}$ and $2.63 \cdot 10^{-4}$, and $1.66 \cdot 10^{-4}$ and $2.81 \cdot 10^{-4}$ respectively. The strain values presented at the top of both models are very alike and do not differ very much. In the lower parts, the strains in both kinds of lamellae stabilize, become constant and equal respectively $2.63–3.92 \cdot 10^{-4}$ for the model with spherical and $2.81–3.96 \cdot 10^{-2}$ for the model with ellipsoidal inclusions. They can be approximated to 0.3-0.35 millistrains and is much smaller than in the model presented earlier.

In Figure 29, the cross-sectional strain distribution in the osteocytes are presented. As explained, in the top region higher strains can be noticed which are the results of the material parameters. Although the strains of osteonal corpus are much lower than those obtained for the model presented earlier, the strains inside the osteocytes still remain relatively high. For the spherical inclusion maximal obtained strains are equal to $1.50 \cdot 10^{-3}$ while for the ellipsoidal they are even higher and equal to $1.78 \cdot 10^{-3}$. These strains can be approximated to 1.5 and 1.78 millistrains, respectively. Here the obtained values are slightly smaller than those in the previous example but it must be also pointed out that the strains detected in osteonal corpus are about twice smaller than those in the previous example. Assuming the osteonal corpus strains are clearly smaller than in the previous example, the strains in the osteocyte stays on the very high level and still remains much higher than those obtained in Lenz and Nackenhorst (2003). Again, the strain detection in ellipsoidal osteocytes resulted in highest values and turned out to be the most efficient.

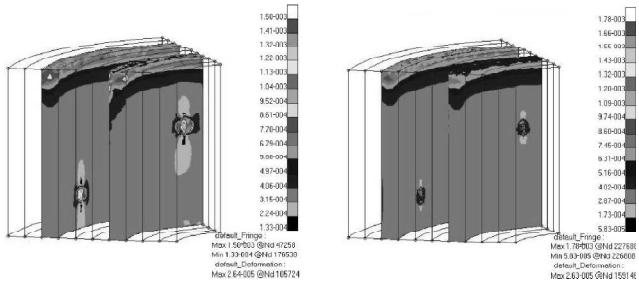

Figure 29: The cross-section strains of spherical (left) and ellipsoidal (right) osteocytes

3. Models Including Lamellae with Twisted Fiber Orientation

In the models presented by Giraud-Guille (1988), the parallel collagen fibrils continuously rotate by a constant angle from plane to plane in a concentric structure (Table 4). The orthogonal material tensors take the values from **C** (–45°) for the first lamella to **C**(+90°) for the last one with increase of 15° for every following lamella layer.

In Figure 30 the displacements of the osteon model with spherical and ellipsoidal osteocytes are presented.

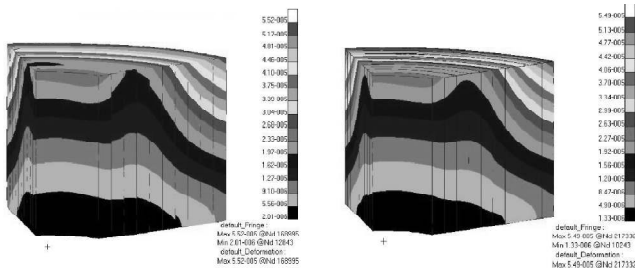

Figure 30: The displacements of the model with spherical inclusions (left) and with ellipsoidal inclusions (right)

In Figure 30 the characteristic behavior can be noticed. As already explained previously, the more the fiber orientation angle differs from 0° location, the more the displacements of the lamella are larger. Accordingly the smallest displacement would be the one with fiber angle of 0° and the softest one, with largest displacement respectively, would be the one with angle of 90°. This property is clearly visible on Figure 30. The 4^{th} lamella described by the material tensor **C**(0°) has the smallest displacements while the last, 10^{th} lamella, with the material tensor **C**(90°) has the highest displacements. With increase of the fiber angle, no matter if in positive or negative direction, the lamellae displacements are getting larger. In the lower half of the model the displacement's distribution is more stabilized and grows with increasing radius. Both displacement distributions and the values presented in Figure 30 are quite similar. For the model with spherical inclusions these values vary between $5.52 \cdot 10^{-2}$ and $2.01 \cdot 10^{-3}$ micrometers, while for the model with ellipsoidal inclusions between $5.49 \cdot 10^{-2}$ and $1.33 \cdot 10^{-3}$, respectively. In this last example it is again shown, that the inclusion shape does not affect the global displacements in a significant way.

According to the above description a characteristic strain distribution field could be expected. Taking into consideration the material properties, their stiffness and the type of example, the strain distributions in the top region of the model should behave in a similar way as the displacements. The softer material under the loading undergoes higher strains than the stiffer one. All these issues are confirmed in Figure 31, which presents the strain distribution for both models, on the left with spherical and on the right with ellipsoidal inclusions.

The strains presented in Figure 31 shows the expected properties. The strain values in the stiffest lamella (4^{th} lamella with fiber orientation 0°) are the smallest while for the softest ones (the last 10^{th} lamella with fiber orientation 90°) are the highest. The characteristic of the distribution of the strain field is congenial to the displacement field. According to the material parameters like the lamellae stiffness, the strains in osteonal corpus vary between $2.60 \cdot 10^{-4}$ and $8.66 \cdot 10^{-4}$

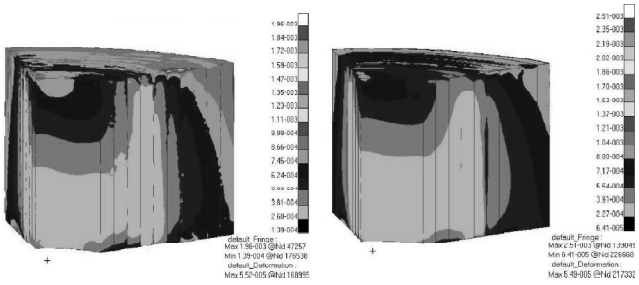

Figure 31: The strains of the osteonal corpus with twisted fiber orientation for spherical (left) and ellipsoidal (right) osteocytes

for the models with spherical inclusions, and between $2.27 \cdot 10^{-4}$ and $8.80 \cdot 10^{-4}$ for the model with ellipsoidal inclusions (see also Figure 31). These values can be approximated to 0.3-0.9 and 0.25-0.9 millistrains, respectively. The higher strains (0.9 millistrains) appear in the softer lamellae while the strains in the stiffer ones stay on a lower level (0.3 millistrains).

The last Figure 32 presents the cross-sectional view of the strains in both kinds of osteocytes. Although the strains in osteonal corpus vary because of the different material parameters of each lamella, the strains in the osteocytes still remain much higher. The presented

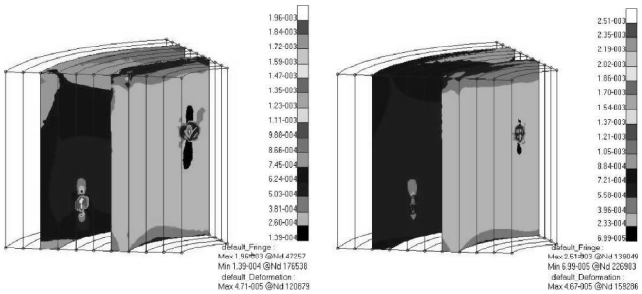

Figure 32: The strains in 4^{th} and 8^{th} lamella with reference to the values in spherical (left) and ellipsoidal (right) osteocytes

lamellae have material parameters of $C(0°)$ (the 4^{th} lamella) and $C(+60°)$ (8^{th} lamella). The strains detected in osteocytes located in the 4^{th} lamella are smaller than those detected in the 8^{th} lamella, but still remain visibly higher than the strains in the osteonal corpus. The maximal strain values for the spherical inclusions is $1.96 \cdot 10^{-3}$ and for the ellipsoidal inclusions is $2.51 \cdot 10^{-3}$.

In the last example it is shown again, the independence of the kind of material properties that the lamella has, the strains in the osteocytes always remain much higher. The strains detected by the ellipsoidal inclusion are larger in all the three presented models. Probably this kind of geometry is closer to the real biological shape and suits better for the mechanical simulations.

4. Summary of the obtained Results

The numerical analysis of all models were carried out. The obtained results confirmed important properties for the osteon and showed interesting behavior for some layers with specific material properties. The advantages of the detailed modeling are also pointed and discussed later in this section. The summary of the obtained strains is presented in Table 6.

Table 6
Strains obtained from the analysis

Fiber orientation	*Shape of the Osteocytes*	*Strains in Osteonal Corpus*	*Max Strains in Osteocytes*
±45°	Sphere	$5.79–6.76 \cdot 10^{-4}$	$1.65 \cdot 10^{-3}$
±45°	Ellipse	$6.44–8.12 \cdot 10^{-4}$	$2.66 \cdot 10^{-3}$
0; 90°	Sphere	$2.63–3.92 \cdot 10^{-4}$	$1.50 \cdot 10^{-3}$
0; 90°	Ellipse	$2.81–3.96 \cdot 10^{-4}$	$1.78 \cdot 10^{-3}$
–45° / (+15°) / + 90°	Sphere	$2.60–8.66 \cdot 10^{-4}$	$1.96 \cdot 10^{-3}$
–45° / (+15°) / + 90°	Ellipse	$2.27–8.80 \cdot 10^{-4}$	$2.51 \cdot 10^{-3}$

For all of the models the main contribution to the total strain derives from the longitudinal (ε_z) strain component (as was suggested by Cowin (2001) or Lenz (2005)) which always had nearly the same value as the total strain. The influence of the other strain components is much smaller.

According to the previous investigation (Lenz and Nackenhorst (2003)) the strain detection obtained by the osteoctes improved. The two hexagonal elements approximating the osteocyte in Lenz and Nackenhorst (2003) detected 1.15 millistrains (with the same loading, boundary condition etc. and for the ±45° fiber orientation), while in this work the spherical osteocytes detected 1.65 millistrains and ellipsoidal even 2.66 millistrains. The results of this research satisfy the pure strain theory by [?], according to which the results are interpreted. It is shown in Table 6 that the values obtained in the osteocytes are much higher than the values in osteonal corpus, and fulfill the required minimum (Frost (1992)) of 1.5 millistrains to send the remodeling signal to the BMU groups.

The total osteon stiffness can be approximated to $9.2 GPa$ which gives good correlation with the measured values by Ascenzi and Bonucci (1968) ($7.3 – 9.5\ G\ Pa$)

10. SUMMARY AND CONCLUSIONS

The mechanosensation process describes the bone physiological reactions. They are coupled with the biomechanical signals produced by the osteocytes under mechanical deformation. The detailed knowledge of all processes occurring in micro scale gives the opportunity to describe more exactly the bone remodeling algorithms which might be of a great importance for healing the fractures and osteoporosis.

The mechanical simulation of a single osteon which denotes the properties of the compact bone is presented

in the beginning of this paper. The analysis is done on the micro length scale. The aim of the possibly close approximation of a real biological geometry is obtained. The three dimensional model of a single osteon is created and computed with the linear elastic theory. The geometry of the osteocytes is generated in two different approaches, according to the data obtained in the literature, as spherical and ellipsoidal inclusions. In comparison with previous research in the mechanosensation and biomechanical field, the presented geometry of the model better describes the biological reality. Six different models are created and computed.

The deformations, strains and stresses inside of a single osteon are calculated with the use of the finite element method and according to the linear elastic analysis. It is shown, that nonlinear computations give the same results as the linear analysis. The model is discretized with relatively a fine mesh. The mesh differences resulting from different shapes of the osteocytes are shown and discussed. The discretisation process is carried out using the tetrahedral elements. These elements are described using the quadratic shape functions.

The material parameters on the nano scale are found in the literature. MORI-TANAKA homogenization method is applied in this work. This transformation, which combines nano and micro scales, results in the material parameters on the micro scale which are presented as an orthogonal material tensor. These calculations are carried out and taken from Lenz and Nackenhorst (2003). All the necessary steps to understand and follow the process, including theoretical background, are presented. The resulting orthotropic material is the function of the mineralization level of the lamellae. These homogenization methods allow one to describe the model parameters which are very close to the realistic biological properties.

The shape of the osteocyte inclusions has a very important role for the strain detection in the bone tissue. In all computations the detected strains are always the highest for the ellipsoidal inclusions. Comparing all the obtained results in this and in other research, where the osteocytes are described with two hexagonal elements, it can be suggested that the ellipsoidal shape is the proper way to describe the biological geometry.

The improvement of the geometry describing the osteocytes provided the required minimum of the pure strain theory presented by Frost (1992). Both, spherical and ellipsoidal osteocytes reached at least the value of 1.5 millistrains in this mechanosensation process. It means that under such a specific loading the osteocytes would send the remodeling signal to the other bone cells in the bone tissue. The previous research with values of 1.15 millistrains, where the osteocytes did not reflect the real biological geometry (Lenz and Nackenhorst (2003)), did not meet the required minimum. This additionally points the importance of preciseness in the geometry modeling approach.

Detailed comparisons with data from the literature and previously carried experiments is given in this work. The main contribution to the total strain derives from the osteon longitudinal (ε_z) strain component which always has nearly the same value as the total strain. The influence of all the other strain components is much smaller.

The micro-length scale simulations show the importance of the modeling approach. It is shown that more satisfactory results are obtained only with more precise description of the biological geometry. The results of this work are of a big importance for further investigation. Especially bridging the micro and meso length scales or attempting the possible exact description of the bone properties on meso scale can be carried with use of results presented here. This work provides some contribution to the progress in the development of the biomechanical field of study.

NOTE

1. Strains are reported in units of microstrain, with 10000 microstrain = 1% change in length.

REFERENCES

Altenbach, J. and Altenbach, H. (1994), *Einführung in die Kontinuumsmechanik*, Teubner.

Ascenzi, A. and Bonucci, E. (1968), 'The compressive properties of single osteons', *Anat. Rec.* **161**, 377-391.

Betten, J. (1993), *Kontinuumsmechanik*, Springer.

Burger, E. H. and Klein-Nulend, J. (1999a), 'Mechanotransduction in bone - role of the lacuno-canalicular network', *The FASEB Journal* **13**, S101-S112.

Burger, E. H. and Klein-Nulend, J. (1999b), 'Responses of bone cells to biomechanical forces in vitro', *Adv Dent Res* **13**, 93-98.

Burger, E. H. and Veldhuijzen, J. (1993), 'Influence of mechanical factors on bone formation, resorption and growth in vitro', *Bone* **7**, 37-56.

Burr, D., Milgrom, C., Fyhrie, D., Forwood, M., Nyska, M., Finestone, A., Hoshaw, S., Saiag, E. and Simkin, A. (1996), 'In vivo measurement of human tibial strains during rigorous activity', *Bone* **18**, 405-410.

Cowin, S. C. (1999), 'Survey article: Bone poroelasticity', *J. of Biomechanics* **32**, 217-238.

Cowin, S. C. (2001), *Bone Mechanics Handbook*, CRC Press, New York.

Cowin, S. C. (2002), 'Mechanosensation and "uid transport in living bone', *J. of Musculoskel Neuron Interact.* **2**(3), 256-260.

Doblare, M. and Garcia, J. (2002), 'Anisotropic bone remodelling model based on a continuum damage-repair theory', *J. of Biomechanics* **35**, 1-17.

Duncan, R. L. and Turner, C. (1995), 'Mechanotransduction and the functional response of bone to mechanical strain', *Calcif. Tissue Int.* **57**, 344-358.

Ebbecke, B. and Nackenhorst, U. (2003), 'Numerical studies on the biocompatibility of inno-vative hip-joint-prostheses', *conference paper, The Finite Element Method in Biomedical Engineering, Biomechanics and Related Fields*, pp. 14-31.

Eshelby, J. D. (1957), 'The determination of the elastic field of an ellipsoidal inclusion, and related problems', *Proceedings of the Physical Society* **A241**, 276-303.

Forwood, M. R. (1996), 'Inducible cyclooxygenase (cox-2) mediates the induction of bone formation by mechanical loading in vivo', *J. Bone Miner. Res.* **11**, 1688-1693.

Fritton, S. P., Beno, T., Ciani, C. and Doty, S. B. (2004), 'Osteocyte lacunar and canaliculi structure'.

Frost, H. (1992), 'Perspectives: bone's mechanical usage windows', *Bone Minerals* **19**, 257-271.

Giraud-Guille, M. M. (1988), 'Twisted plywood architecture of collagen fibrils in human compact bone osteons', *Calcif. Tissue Int.* **42**, 167-180.

Grass (2005), 'Human anatomy and physiology', *http://lrn.org*.

Kaspar, D., Seidel, W., Neidlinger-Wilke, C., Ignatius, A. and Claes, L. (2000), 'Dynamic cell stretching increases human osteoblast proliferation and cicp synthesis but decreases osteocalcin synthesis and alkaline phosphatase activity', *J. of Biomechanics* **33**, 45-51.

Korenstein, R., Somjen, D. and Fischler, H. (1984), 'Capacitative pulsed electric stimulation of bone cells. induction of cyclic-amp changes and dna syntheses.', *Biochim. Biophys. Acta* **803**, 302-307.

Lenz, C. (2005), 'Numerical micro-meso modeling of mechanosensation driven osteonal re-modeling in cortical bone', *Doktor Work* pp. 91-102.

Lenz, C. and Nackenhorst, U. (2003), 'Finite element analysis of osteons concerning the mechanosensation of bone material', *conference paper*, *The Finite Element Method in Biomedical Engineering, Biomechanics and Related Fields* pp. 91-102.

Martin, R., Burr, D. and Sharkey, N. (1998), *Skeletal Tissue Mechanics*, Springer.

Mullender, M. G., van der Meer, D. D., Huiskes, R. and Lips, P. (1996), 'Osteocyte density changes in aging and osteoporosis, *http://alexandria.tue.nl/repository/freearticles/585485.pdf*', Web Page, Bone Vol. 18, No. 2.

Murray, D. W. and Rushton, N. (1990), 'The effect of strain on bone cell prostaglandine e2 release: a new experimental method', *Calcif. Tissue Int.* **47**, 35-39.

Neidlinger-Wilke, C., Stall, I., Claes, L., Brand, R., Hoellen, I., Rubenacker, S., Arand, M. and Kinzl, L. (1995), 'Human osteoblasts from younger normal and asteoporotic donors show differences in proliferation and tgf β release in response to cyclic strain', *J. Biomechanic* **28**, 1411-1418.

Owan, I., Burr, D., Turner, C., Qiu, J., Tu, Y., Onyia, J. and Duncan, R. (1997), 'Mechan-otransduction in bone: osteoblasts are more responsive to "uid forces than mechanical strain', *Am. J. Physiol.* **273**, C810-815.

Pollack, S. R. and Petrov, N. (1984), 'An anatomical model for streaming potentials in osteons', *J. of Biomechanics* **17**, 627-636.

Rho, J. Y., Kuhn-Spearing, L. and Zioupos, P. (1998), 'Mechanical properties and the hierarchical structure of bone', *Medical Engineering and Physics* **20**, 92-102.

Rubin, C. T. (1984), 'Skeletal strain and the functional significance of bone architecture', *Calcif. Tissue Int.* **36**, 11-18.

Rubin, C. T., Judex, S. and Hadjiargyrou, M. (2002), 'Skeletal adaptation to mechanical stimuli in the absence of formation and resorption of bone', *J. of Musculoskel Neuron Interact.* **2**, 264-267.

Turner, C. H., Forwood, M. R., Rho, J. Y. and Yoshikawa, T. (1994), 'Mechanical loading thresholds for lamellar and woven bone formation', *J. Bone Miner. Res.* **9**, 87-97.

Turner, C. H. and Pavalko, F. M. (1998), 'Mechanotransduction and functional response of the skeleton to physical stress: The mechanisms and mechanics of bone adaptation', *J. Orthop Science.* **3**, 346-355.

v. d. Meulen, M. C. H. and Prendergast, P. J. (2000), 'Mechanics in skeletal development, adaptation and disease', *Phil. Trans. R. Soc. Lond.* **358**, 565-578.

Wang, L., Fritton, S. P., Weinbaum, S. and Cowin, S. C. (2003), 'On bone adaptation due to venous stasis', *J. of Biomechanics* **36**, 1439-1451.

Wolff, J. (1986), 'The law of bone remodelling', *Springer*.

Wriggers, P. (2001), *Nichtlineare Finite-Element-Methoden*, Springer.

You, J., Yellowley, C. E., Donahue, H. J., Zhang, Y., Chen, Q. and Jacobs, C. R. (2000), 'Substrate deformation levels associated with routine physical activity are less stimulatory to bone cells relative to loading-induced oscillatory fluid flow.', *J. of Biomechanical Engineering* **122**, 387-393.

You, L., Cowin, S. C., Schaer, M. B. and Weinbaum, S. (2001), 'A model for strain amplification in the actin cytoskeleton of osteocytes due to fluid drag on pericellular matrix', *J. of Biomechanics* **34**, 1375-1386.

Zienkiewicz, O. C. and Taylor, R. L. T. (1994), *The finite element method*, Vol. 1, 4 edn, McGraw-Hill. Basic Formulations and linear problems.